Electronic Supplementary Information for

Coordination Modulated On-Off flexibility in a Metal-organic Framework

Jorge Albalad,[a] Ricardo A. Peralta,[a] Michael T. Huxley,[a] Steven Tsoukatos,[a] Zhaolin Shi,[b] Yue-Biao Zhang,[b] Jack D. Evans,[c‡] Christopher J. Sumby*[a] and Christian J. Doonan*[a]

[a] Centre for Advanced Nanomaterials and Department of Chemistry, The University of Adelaide, North Terrace, Adelaide, SA 5000, Australia.

* Email: christopher.sumby@adelaide.edu.au (CJS); christian.doonan@adelaide.edu.au (CJD)

[b] School of Physical Science and Technology, ShanghaiTech University Shanghai, 201210 (China)

[c] Department of Inorganic Chemistry, Technische Universität Dresden, 01062 Dresden, Germany

‡ Current affiliation: Centre for Advanced Nanomaterials and Department of Chemistry, The University of Adelaide, North Terrace, Adelaide, SA 5000, Australia

Table of Contents

S1.0 Main text supporting characterisation

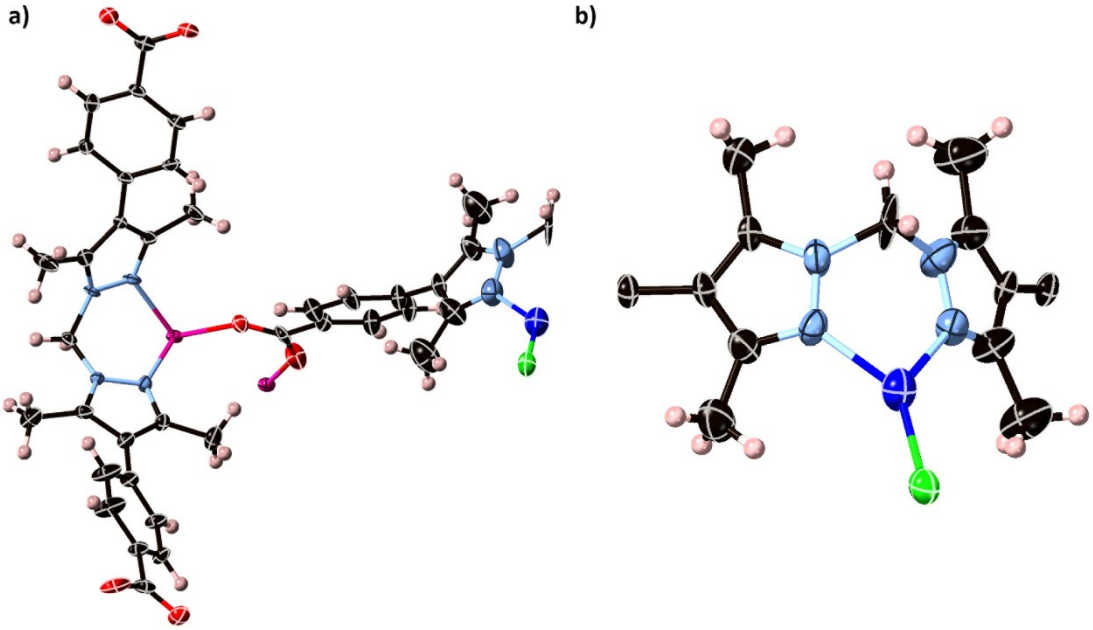

Figure S1. (a) The asymmetric unit of **1**·[CuCl], with all non-hydrogen atoms represented by ellipsoids at the 50% probability level (C, black; H, white; N, light blue; O, red; Cu, dark blue; Mn, pink; Cl, green). Crystallographically resolved solvent molecules (toluene) were removed for clarity. (b) Perspective view of the crystallographically distinct Cu(I) chelation sites with all non-hydrogen atoms represented by ellipsoids at the 50% probability level.

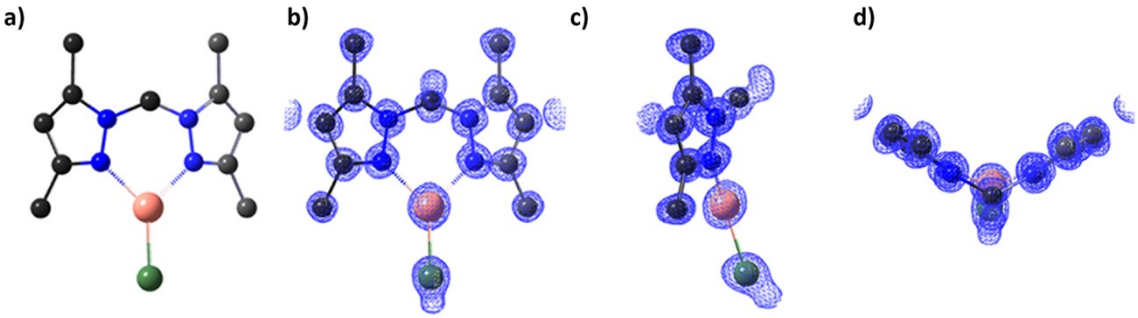

Figure S2. (a) Perspective view of the first chelated Cu(I) complex in **1**·[CuCl], and the overlaid electron density map as viewed from the (b) front, (c) side and (d) top of the complex.

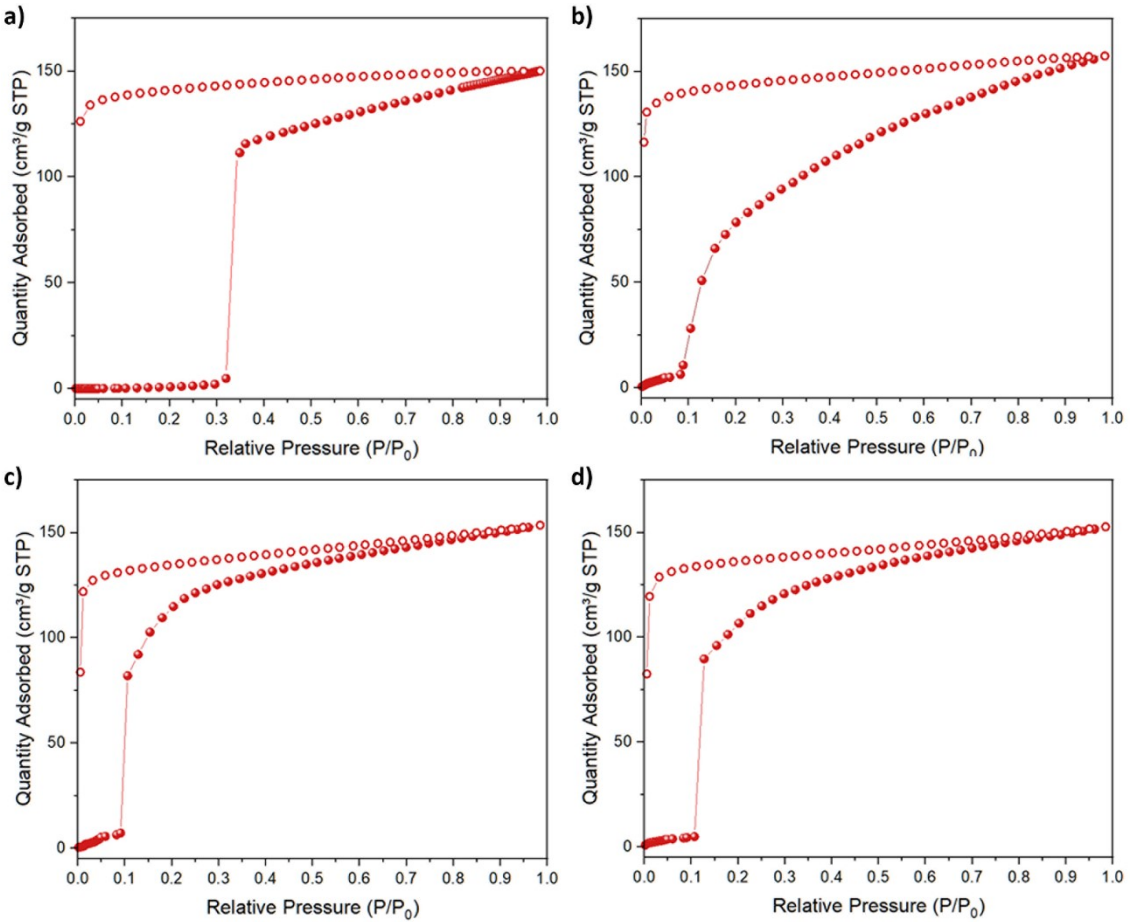

Figure S3. N_2 isotherm data collected on digonal **1**·[CuCl]-*unlocked* at 77 K, after activation at 100 °C for 90 minutes. (a) activated from dry *n*-pentane, (b) activated from dry methanol, (c) activated from dry acetone, and (d) activated from dry diethyl ether. Coloured circles represent adsorption, open circles represent desorption.

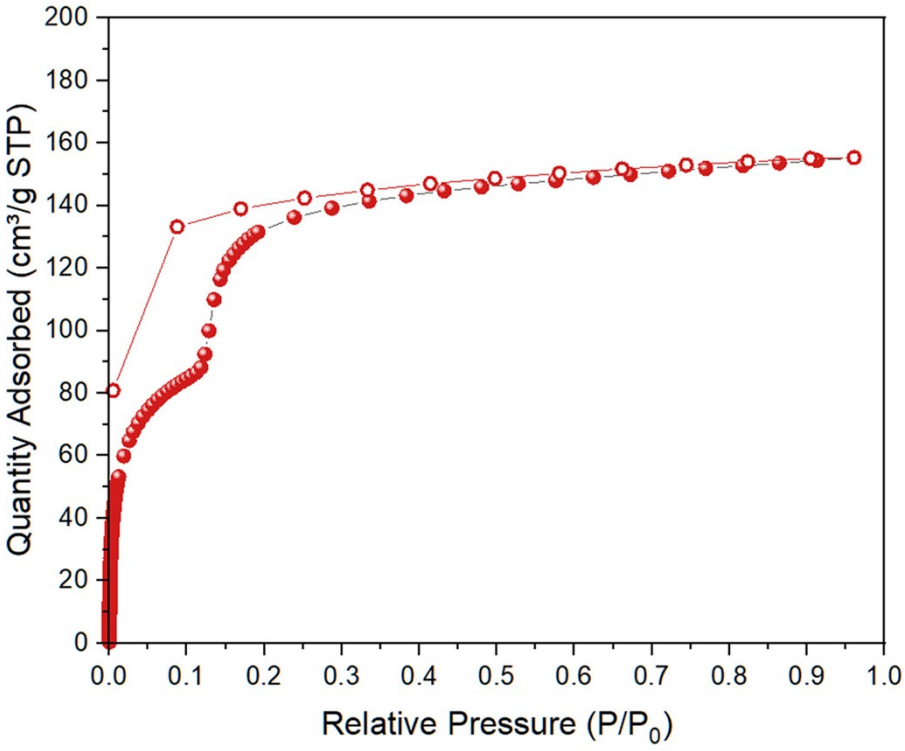

Figure S4. CO_2 isotherm data collected at 195 K on **1**·[CuCl]-*unlocked* after activation from dry *n*-pentane at 100 °C for 90 min. Coloured circles represent adsorption, open circles represent desorption.

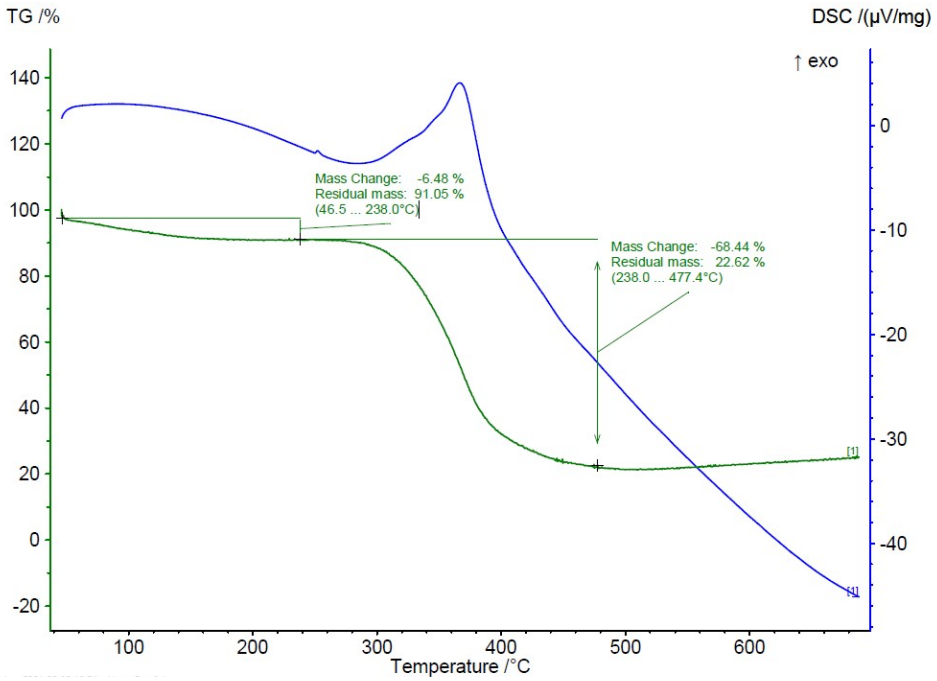

Figure S5. Thermogravimetric analysis spectrum (green) coupled to differential scanning calorimetry analysis (blue) of pre-activated **1**·[CuCl]-*unlocked,* showing the thermal stability of the framework up to 290 °C. The initial mass loss of -6.48 % is attributed to atmospheric moisture adsorbed during sample handling. Analysis conditions: 45 ºC – 700 °C at 5 °C/min, under oxidising (air) atmosphere.

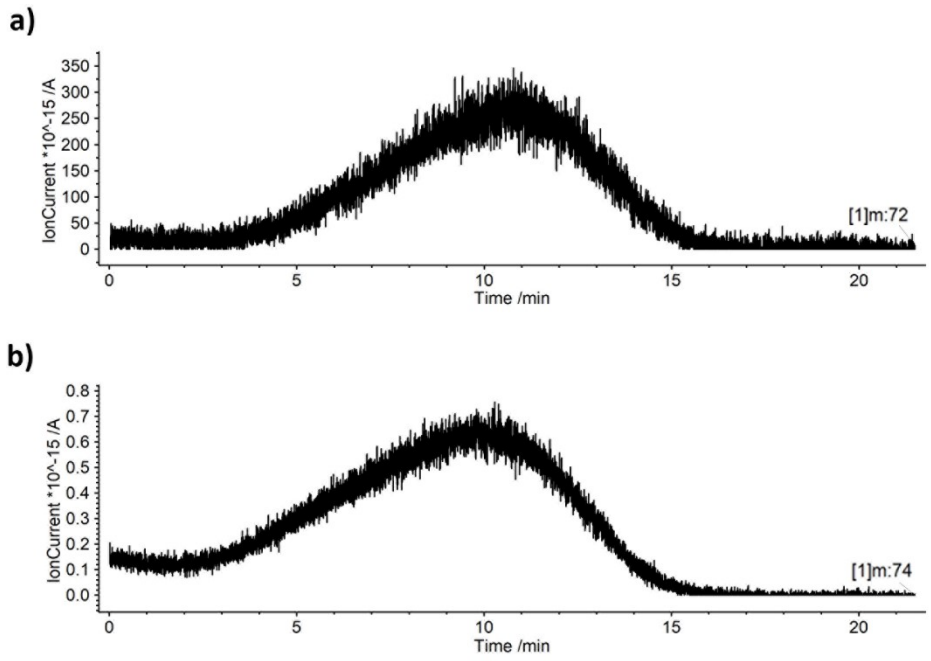

Figure S6. Mass spectra detection counts of residual trapped solvent molecules during the TGA analysis of activated **1**·[CuCl]-*unlocked* from (a) *n*-pentane and (b) diethyl ether ($m/z_{pentane}$ = 72; m/z_{ether} = 74). TGA conditions: 45 °C – 300 °C at 10 °C/min under N_2 flow.

a)

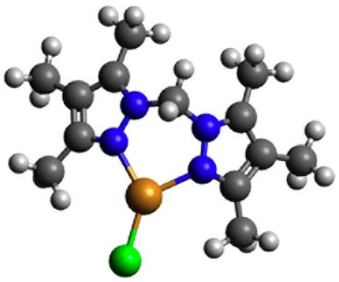

	Cu – X (Å)	Cu – N (Å)
[(CH$_2$(Pyz)$_2$)(Cu-Cl)]	2.155	2.04
[(CH$_2$(Pyz)$_2$)(Cu-Br)]	2.287	2.05
[(CH$_2$(Pyz)$_2$)(Cu-I)]	2.455	2.05

b)

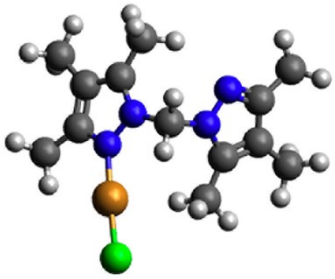

	Cu – X (Å)	Cu – N (Å)
[(CH$_2$(Pyz)$_2$)(Cu-Cl)]	2.008	2.04
[(CH$_2$(Pyz)$_2$)(Cu-Br)]	2.224	2.05
[(CH$_2$(Pyz)$_2$)(Cu-I)]	2.390	2.05

Figure S7. Theoretical model obtained for the bis-pyrazole – Cu – halide system, with the corresponding Cu-X and Cu-N bond distances for (a) trigonal planar (syn) conformation and (b) digonal (anti) conformation. Initial conformations were provided from dihedral scans (N-N-N-N) that used the BP86 density functional[1,2] and efficient coulomb with the chain of spheres exchange algorithms (RIJCOSX).[3] A combination of the def2-SVP[4] for C, N, H atoms and def2-TZVP for Cu and halogens were applied with the def2/J auxiliary basis set for all atoms.[5] These dihedral scans highlight the relative potential energy of the two and three-coordinate forms of the complexes.

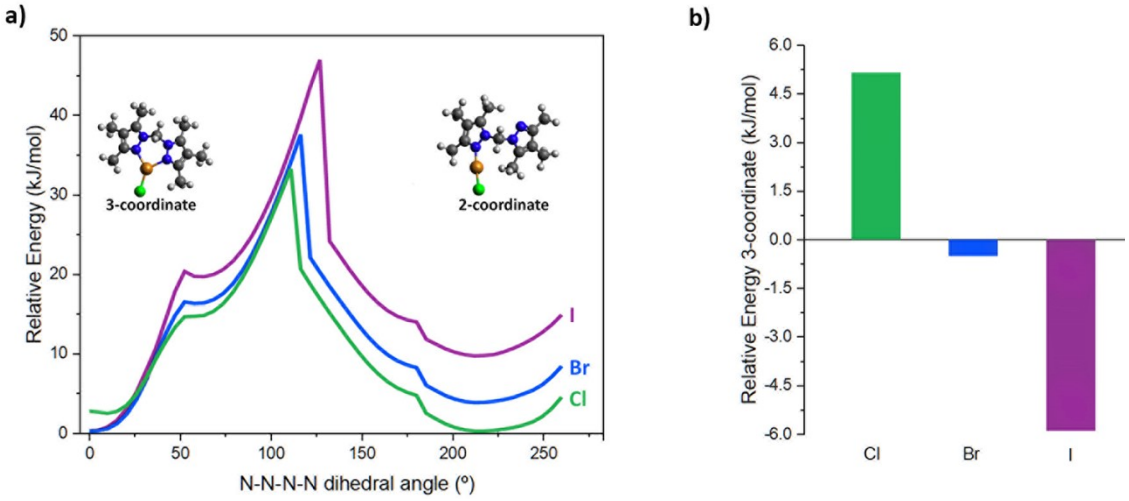

Figure S8. (a) Calculated relative energy levels for the bis-pyrazole – Cu – halide system at different N-N-N-N dihedral angles. (b) Relative energy of the 3-coordinate (trigonal planar) conformation versus the 2-coordinate (linear) conformation for each bis-pyrazole – Cu – halide system. The Cu-Cl complex is clearly favouring a linear conformation, unlike the other Cu-X systems.

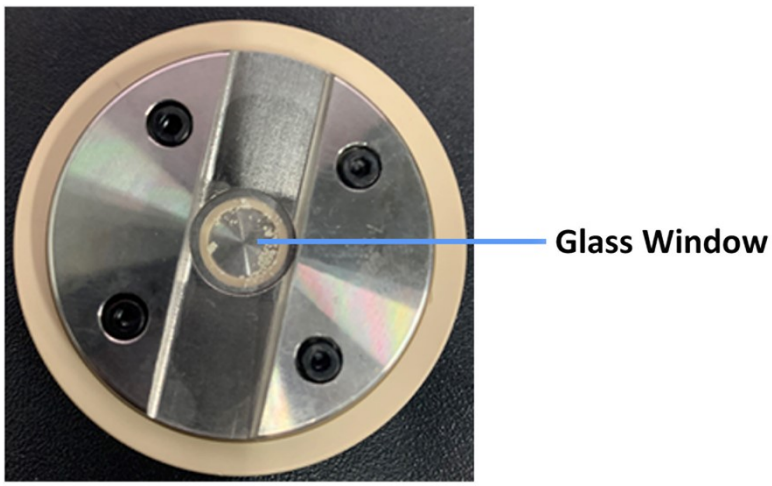

Figure S9. Picture of the used sample cells during **1**·[CuCl] Raman spectroscopy analysis. The glass window, with MOF crystals carefully placed within, is highlighted.

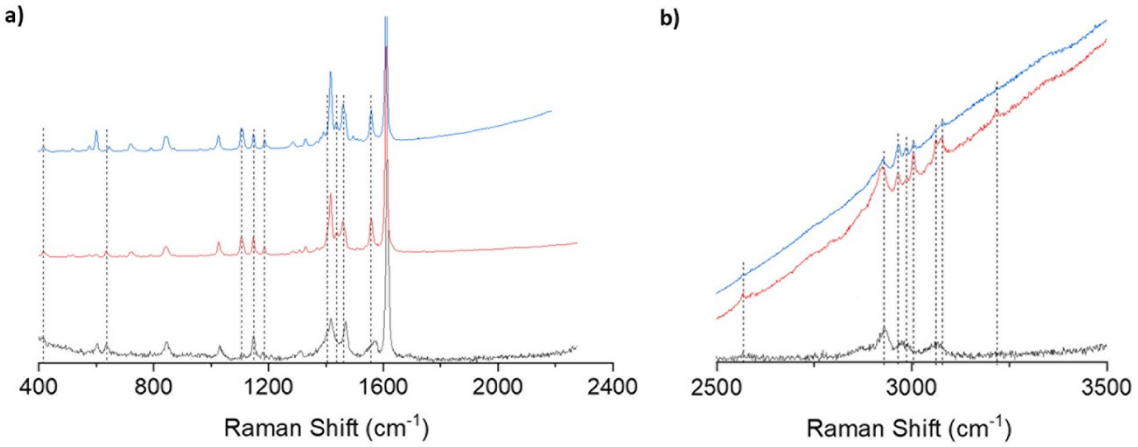

Figure S10. Experimental *in situ* Raman spectra of **1**·[CuCl] at low (a) and high (b) wavenumber regions. Colour scheme: as-made (black), activated (red) and post-isotherm (blue). Assignment of the peaks was precluded by the strong effect/contribution of multiple framework factors, including solvents, aromatic linkers, secondary building units, and pillaring linkers with embedded metal centres. However, a significant change is observed upon activation of 1·CuCl under high temperature and vacuum, which points to an induced phase transition within the framework.

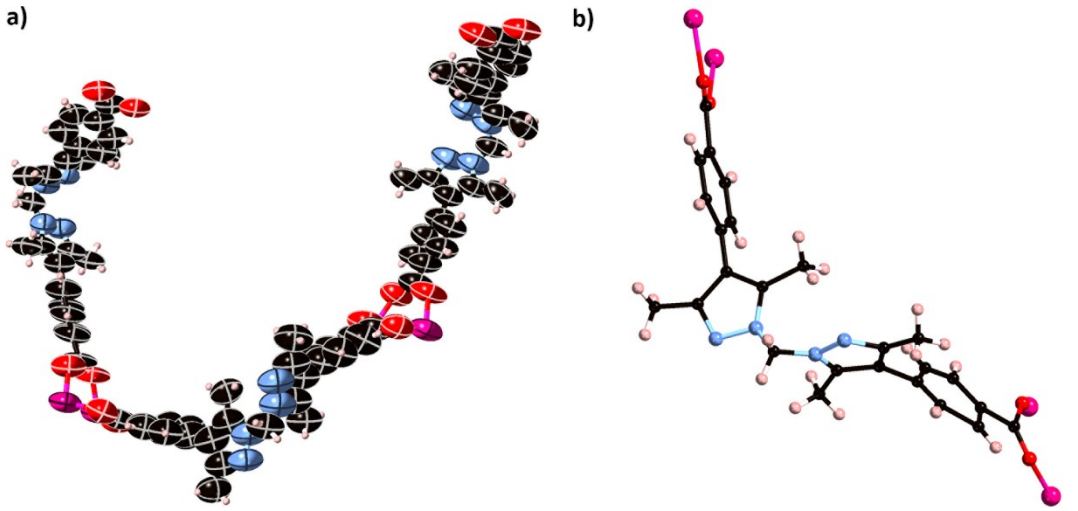

Figure S11. (a) The asymmetric unit of **1**·[CuCl]-*unlocked* after activation at 100 °C from *n*-pentane for 90 min; with all non-hydrogen atoms represented by ellipsoids at the 50% probability level (C, black; H, white; N, light blue; O, red; Mn, pink). The structure shows elevated levels of disorder, which precludes a proper elucidation of the Cu(I) centre. There were no crystallographically resolved solvent molecules in the collected SCXRD data. (b) Ball-and-stick perspective view of the crystallographically disordered bis(pyrazolyl)methane chelation sites, to give a clear insight on their "anti" disposition after activation.

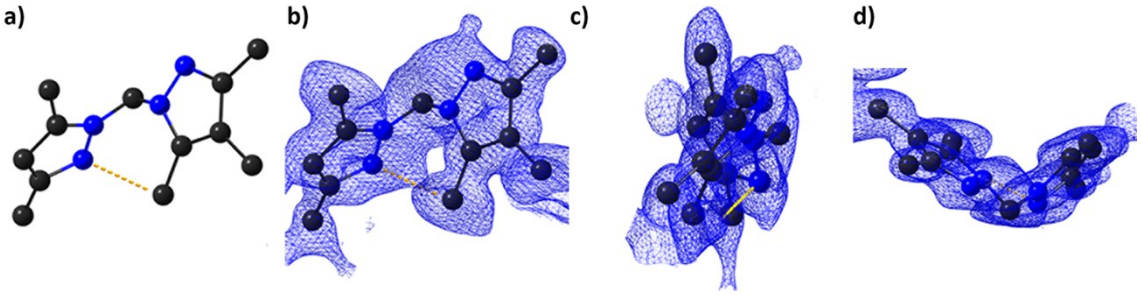

Figure S12. (a) Perspective view of the first chelated Cu(I) complex in **1**·[CuCl]-*unlocked*, and the overlaid electron density map as viewed from the (b) front, (c) side and (d) top of the complex.

Table S1. Cu(I) and associated anion occupancy determined via measurement of the Mn:Cu ratio and the Cu:halide ratio using EDX analysis.

Sample	Cu (at. %)[a,b]	Cl (at. %)[a,b]	Std error (%)
1·[Cu(MeCN)(Cl)]	103.2	108.6	4.2
1·[CuCl]	101.0	105.8	2.4
1·[CuCl]-*unlocked*	106.2	104.2	5.8
1·[CuCl]-*resolv*	105.4	102.7	3.0

[a] Average atomic % obtained from three areas of crystals.
[b] Relative to full occupancy of the bis(pyrazole)methane coordinating sites in **1** (Mn:Cu:X = 3:1:1).

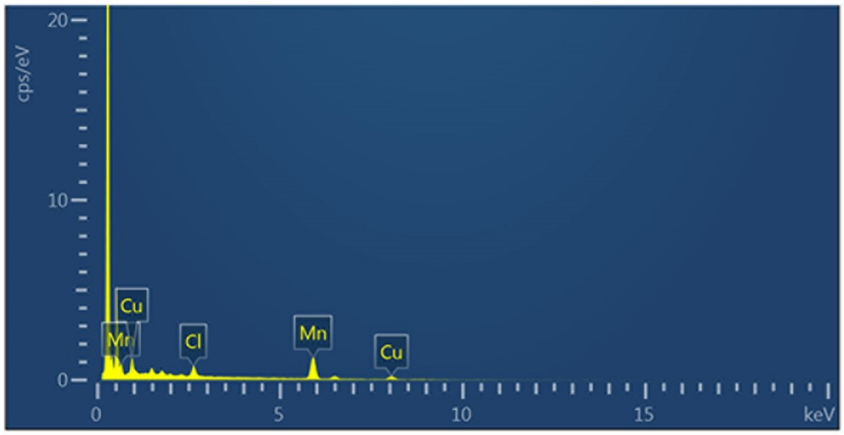

Figure S13. Representative raw EDX spectra for **1**·[CuCl]-*unlocked*,

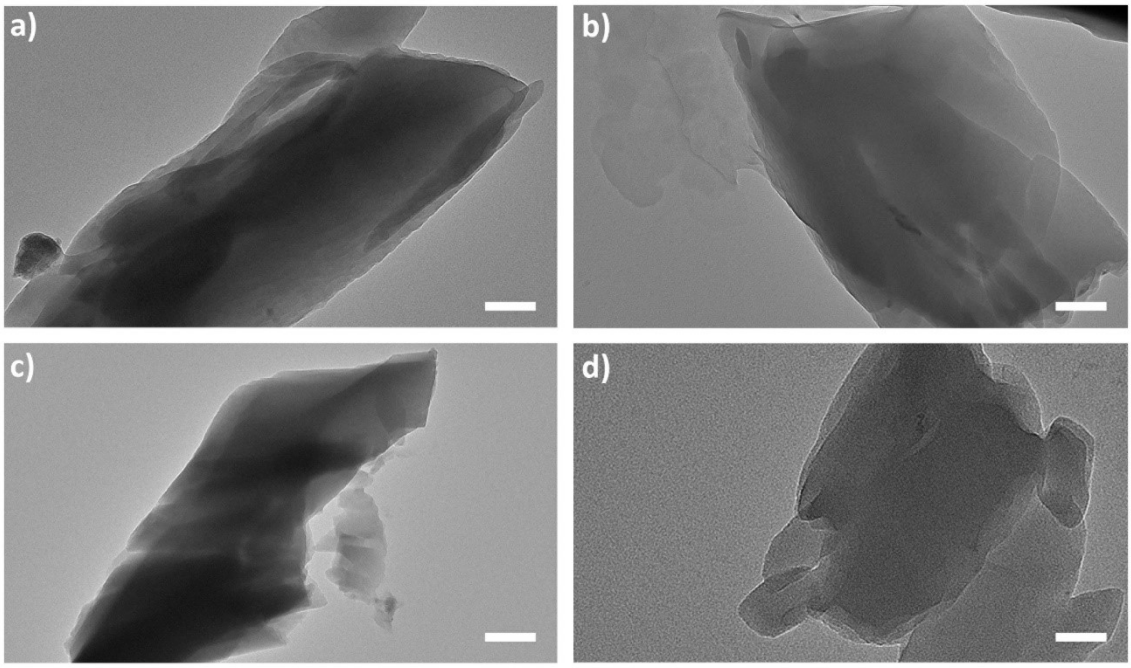

Figure S14. HR-TEM imaging of **1**·[CuCl]-*unlocked* (a-b) and **1**·[CuCl]-*resolv* (c-d) after their respective N_2 adsorption isotherms, confirming that the Cu (I) centres embedded in the MOF are not being decomposed into inorganic Cu/CuOx nanoparticles during sample activation under high temperature/vacuum conditions. Samples were sonicated in methanol for 10 minutes to reduce the crystal size and ensure a proper dispersion for TEM imaging. EDX quantification was not possible due to the strong Cu signal coming from the TEM sample grids. Scale bar: 100 nm.

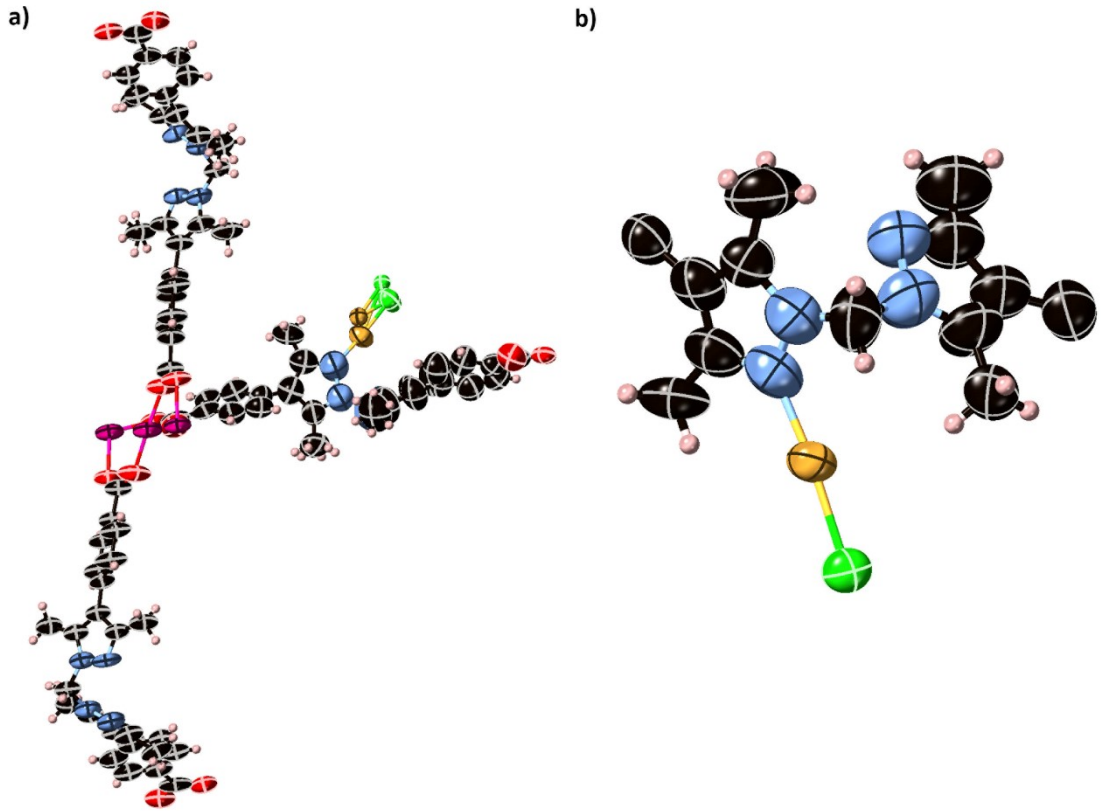

Figure S15. (a) The asymmetric unit of **1**·[AuCl], with all non-hydrogen atoms represented by ellipsoids at the 50% probability level (C, black; H, white; N, light blue; O, red; Au, yellow; Mn, pink; Cl, green). Crystallographically resolved solvent molecules (Toluene) were removed for clarity. (b) Perspective view of the crystallographically distinct Au(I) chelation sites with all non-hydrogen atoms represented by ellipsoids at the 50% probability level. The secondary Au centre was omitted for clarity, but is represented in (a) and in the electron density map of the same structure.

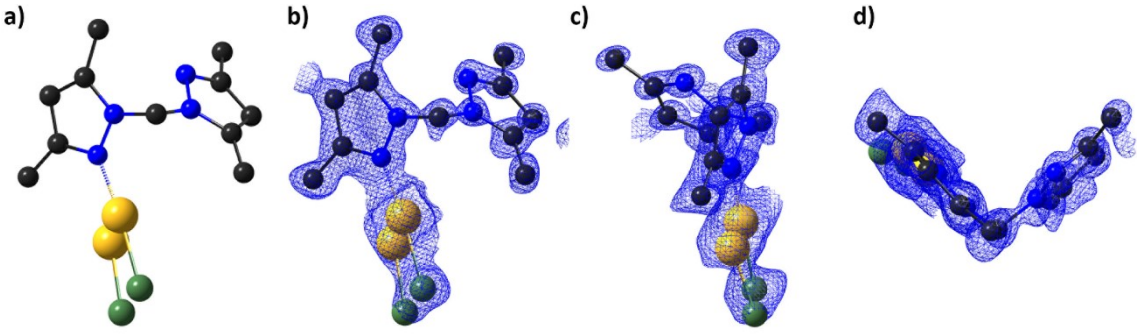

Figure S16. (a,e) Perspective view of the first chelated Au(I) complex in **1**·[AuCl], and the overlaid electron density map as viewed from the (b) front, (c) side and (d) top of the complex.

Table S2. Au(I) and associated anion occupancy determined via measurement of the Mn:Au ratio and the Au:Cl ratio using EDX analysis.

Sample	Au (at. %)[a,b]	Cl (at. %)[a,b]	Std error(%)
1·[AuCl]	104.0	107.5	3.8

[a] Average atomic % obtained from three areas of crystals.
[b] Relative to full occupancy of the bis(pyrazole)methane coordinating sites in **1** (Mn:Au:Cl = 3:1:1).

Figure S17. Representative raw EDX spectra for **1**·[AuCl].

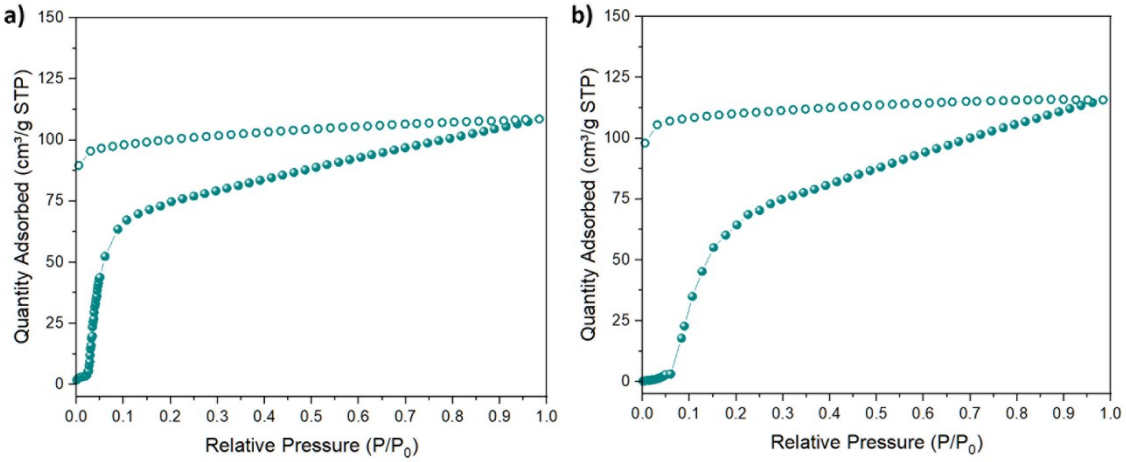

Figure S18. N_2 isotherm data collected on **1**·[AuCl] at 77 K, after activation from (a) dry diethyl ether at room temperature for 90 minutes, and (b) *n*-pentane at room temperature for 90 minutes. Coloured circles represent adsorption, open circles represent desorption.

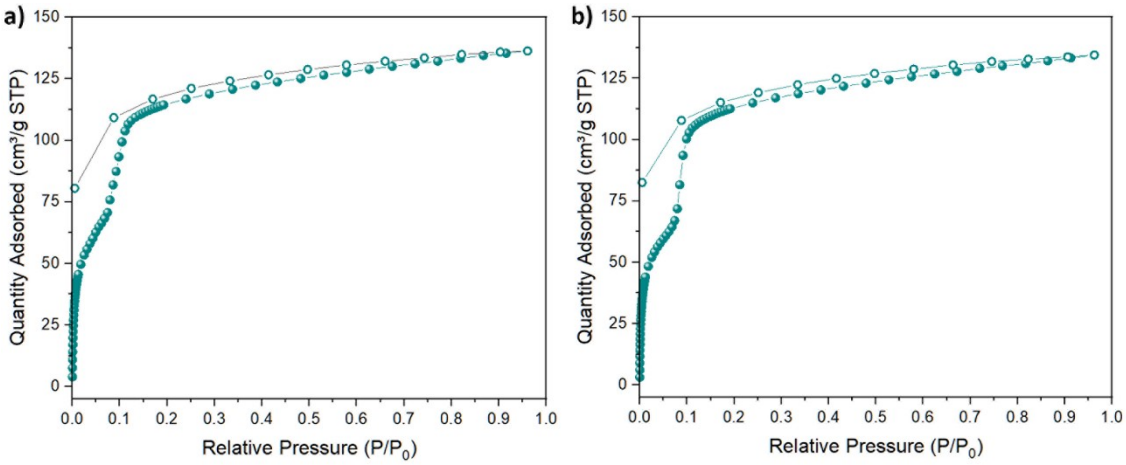

Figure S19. CO_2 isotherm data collected at 195 K on **1**·[AuCl], activated from (a) dry diethyl ether at room temperature for 90 min, and (b) dry *n*-pentane at room temperature for 90 min. Coloured circles represent adsorption, open circles represent desorption.

Table S3. Cu(I) and associated anion occupancy determined via measurement of the Mn:Cu ratio and the Cu:halide ratio using EDX analysis.

Sample	Cu (at. %)[a,b]	Cl (at. %)[a,b]	Br (at. %)[a,b]	I (at. %)[a,b]	Std error (%)
1·[CuCl]	101.0	105.8			2.4
1·[CuBr]	97.8	1.2	110.1		2.1
1·[CuI]	98.7	0.4		104.4	2.5

[a] Average atomic % obtained from three areas of crystals.
[b] Relative to full occupancy of the bis(pyrazole)methane coordinating sites in **1** (Mn:Cu:X = 3:1:1).

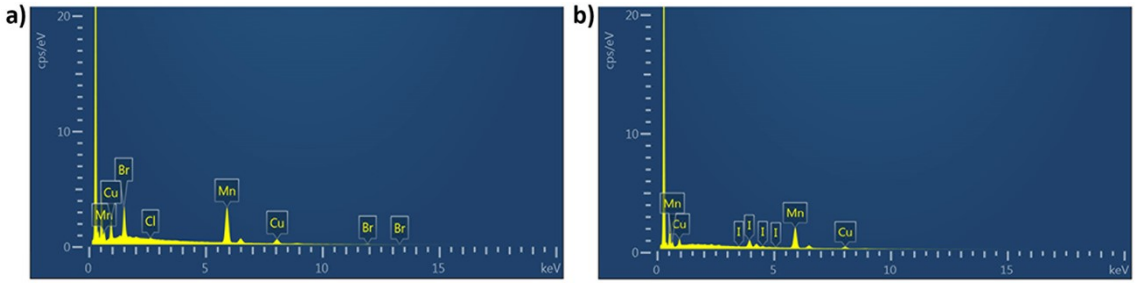

Figure S20. Representative raw EDX spectra for (a) **1**·[CuBr] and (b) **1**·[CuI].

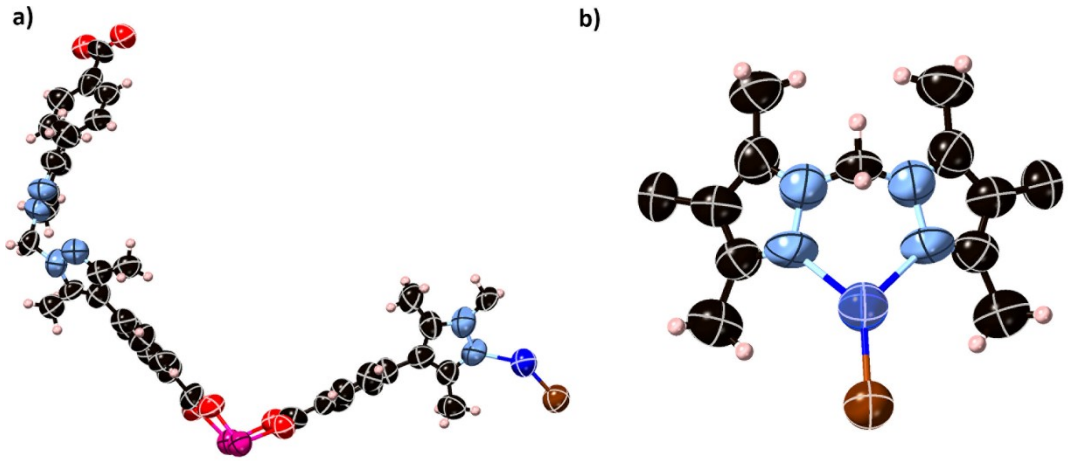

Figure S21. (a) The asymmetric unit of **1**·[CuBr], with all non-hydrogen atoms represented by ellipsoids at the 50% probability level (C, black; H, white; N, light blue; O, red; Cu, dark blue; Mn, pink; Br, brown). Crystallographically resolved solvent molecules (cyclohexane) were removed for clarity. (b) Perspective view of the crystallographically distinct Cu(I) chelation sites with all non-hydrogen atoms represented by ellipsoids at the 50% probability level.

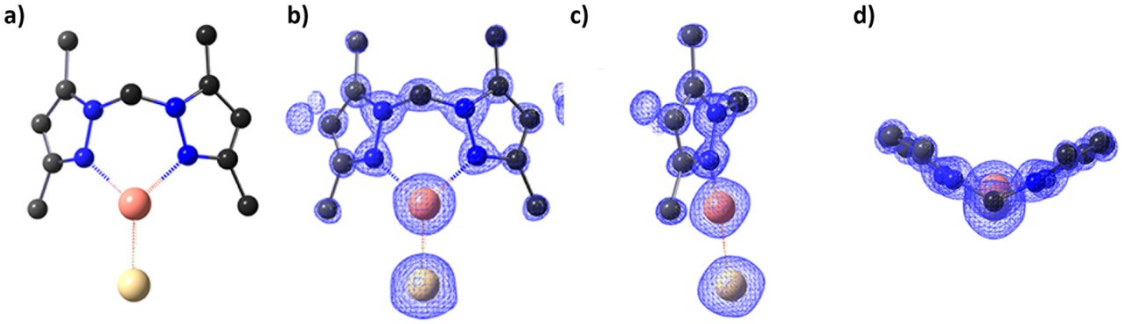

Figure S22. (a) Perspective view of the first chelated Cu(I) complex in **1**·[CuBr], and the overlaid electron density map as viewed from the (b) front, (c) side and (d) top of the complex.

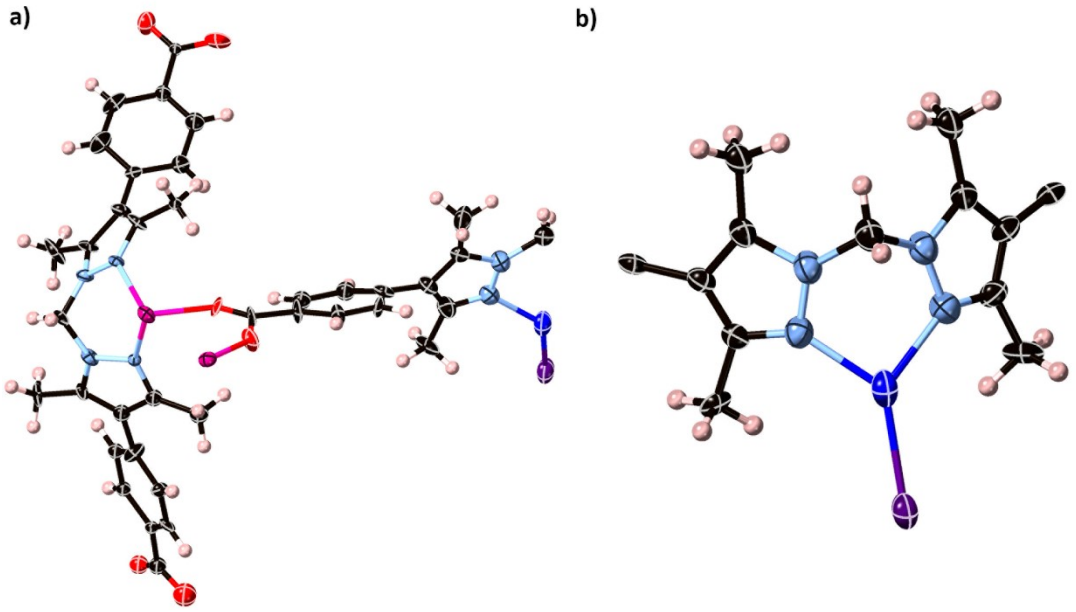

Figure S23. (a) The asymmetric unit of **1**·[CuI], with all non-hydrogen atoms represented by ellipsoids at the 50% probability level (C, black; H, white; N, light blue; O, red; Cu, dark blue; Mn, pink; I, purple). Crystallographically resolved solvent molecules (cyclohexane) were removed for clarity. (b) Perspective view of the crystallographically distinct Cu(I) chelation sites with all non-hydrogen atoms represented by ellipsoids at the 50% probability level.

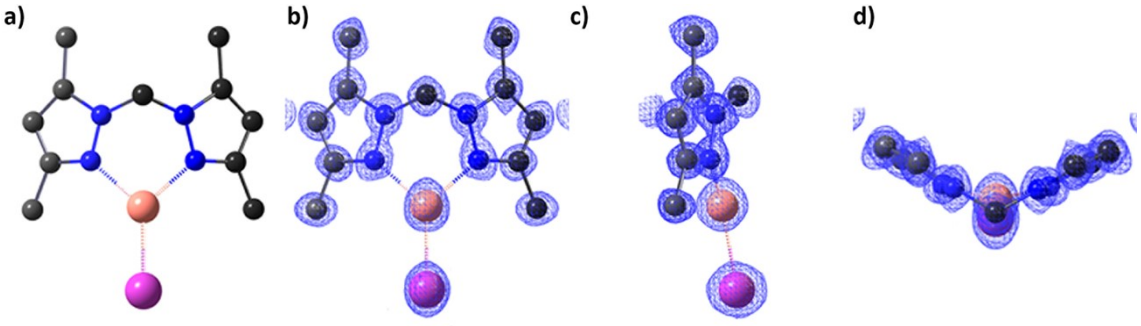

Figure S24. (a) Perspective view of the first chelated Cu(I) complex in **1**·[CuI], and the overlaid electron density map as viewed from the (b) front, (c) side and (d) top of the complex.

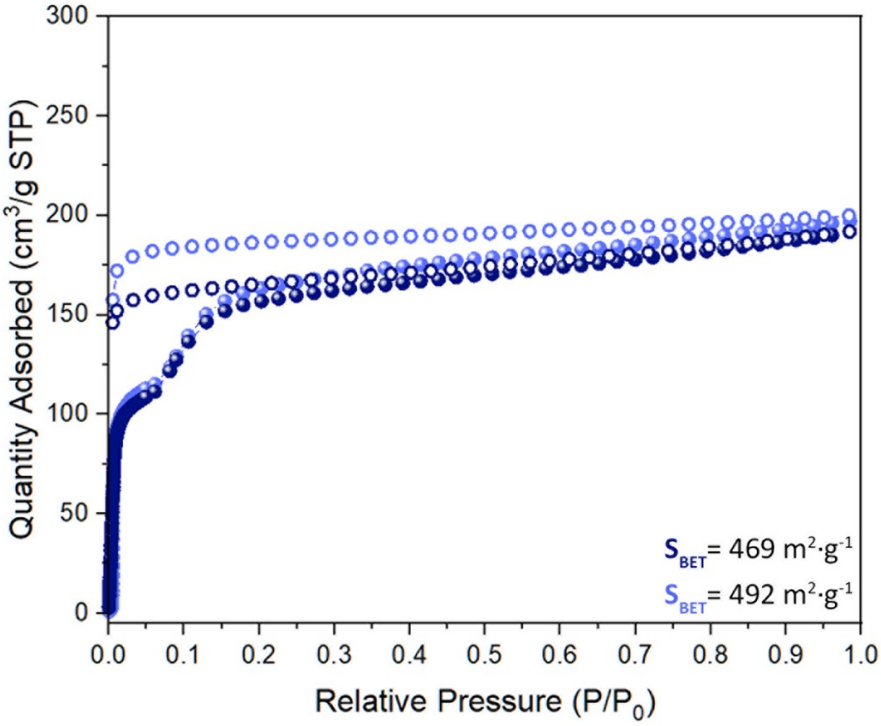

Figure S25. N_2 isotherm data collected on **1**·[CuBr] at 77 K, after activation from dry pentane at room temperature for 90 minutes (dark blue), and at 100 °C for 90 minutes (light blue). Coloured circles represent adsorption, open circles represent desorption.

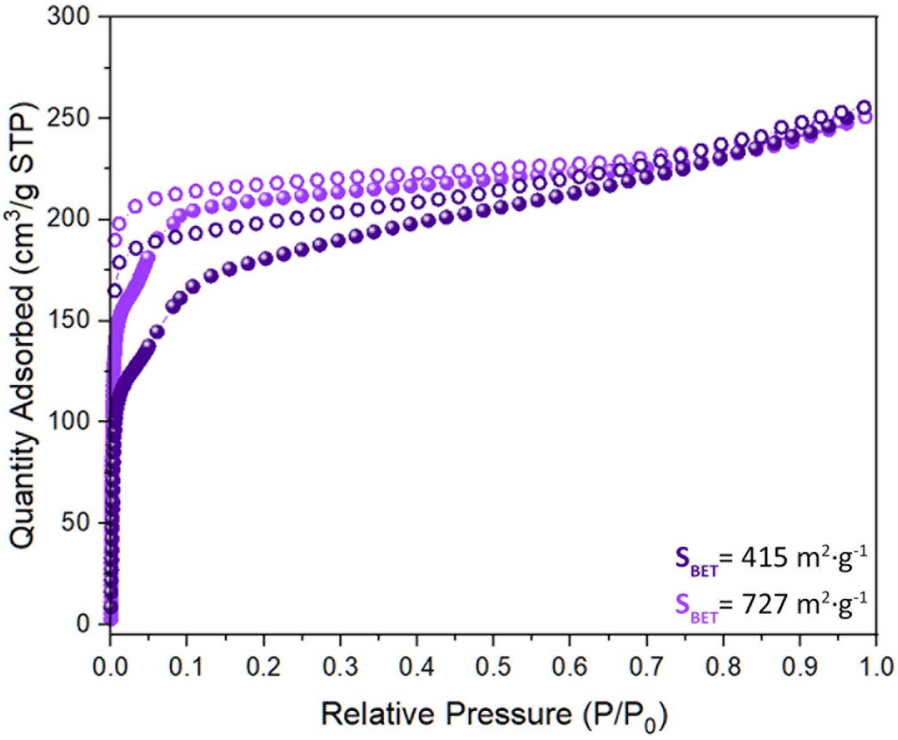

Figure S26. N_2 isotherm data collected on **1**·[CuI] at 77 K, after activation from dry pentane at room temperature for 90 minutes (dark purple), and at 100 °C for 90 minutes (light purple). Coloured circles represent adsorption, open circles represent desorption.

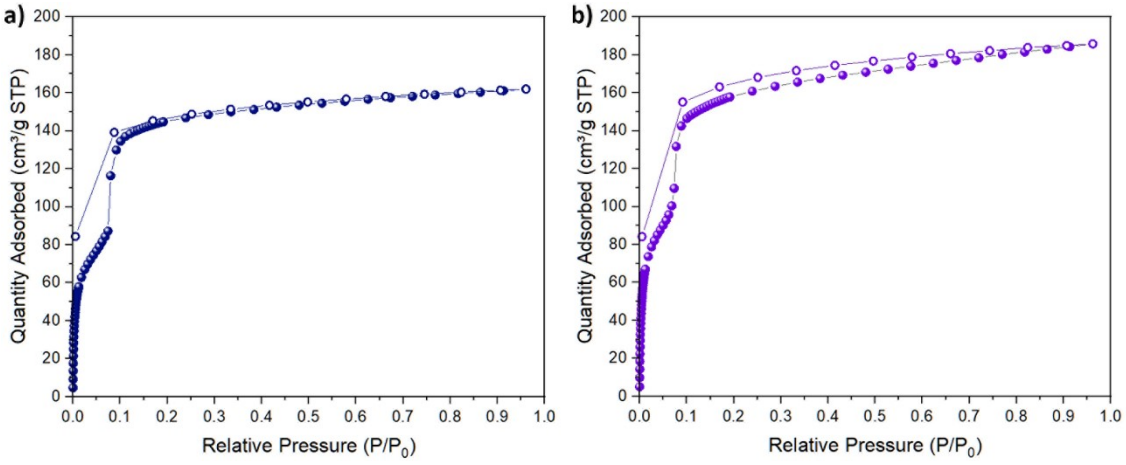

Figure S27. (a) CO_2 isotherm data collected at 195 K on **1**·[CuBr] after activation from supercritical CO_2. (b) CO_2 isotherm data collected at 195 K on **1**·[CuI] after activation from dry *n*-pentane at 100 °C for 90 min. Coloured circles represent adsorption, open circles represent desorption.

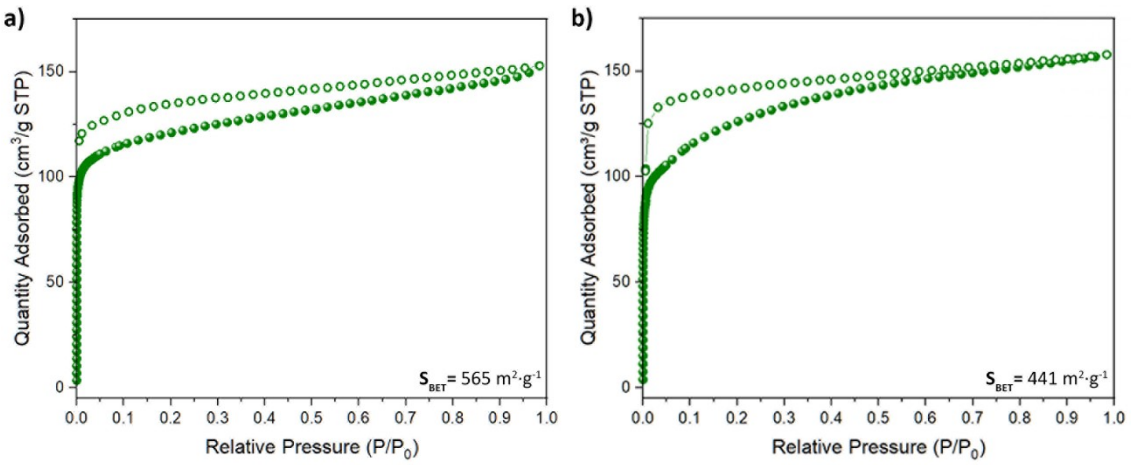

Figure S28. N_2 isotherm data collected on trigonal planar **1**·[CuCl]-*trigonal planar* at 77 K, after activation at room temperature from (a) dry diethyl ether for 90 minutes, and (b) activated from supercritical CO_2. Coloured circles represent adsorption, open circles represent desorption.

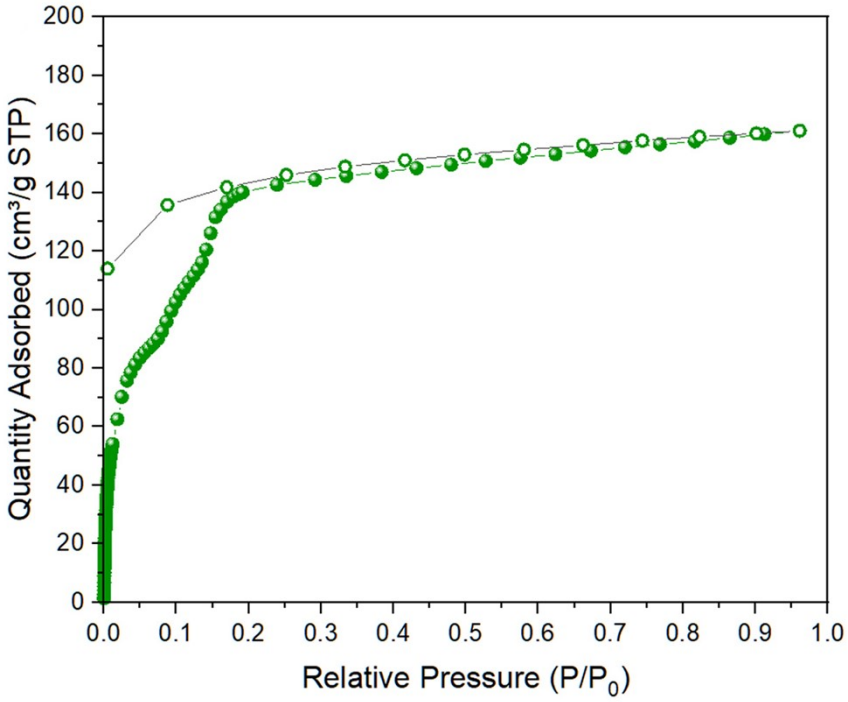

Figure S29. CO_2 isotherm data collected at 195 K on **1**·[CuCl]-*locked* after activation from supercritical CO_2.. Coloured circles represent adsorption, open circles represent desorption.

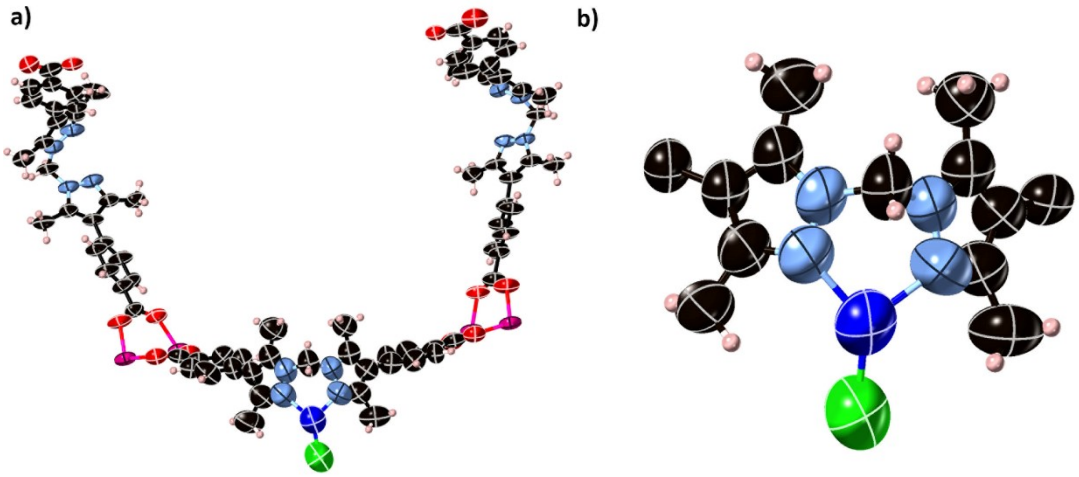

Figure S30. (a) The asymmetric unit of **1**·[CuCl]-*locked* after activation at room temperature from diethyl ether for 90 min; with all non-hydrogen atoms represented by ellipsoids at the 50% probability level (C, black; H, white; N, light blue; O, red; Cu, dark blue; Mn, pink; Cl, green). There were no crystallographically resolved solvent molecules in the collected SCXRD data. (b) Perspective view of the crystallographically distinct Cu(I) chelation sites with all non-hydrogen atoms represented by ellipsoids at the 50% probability level.

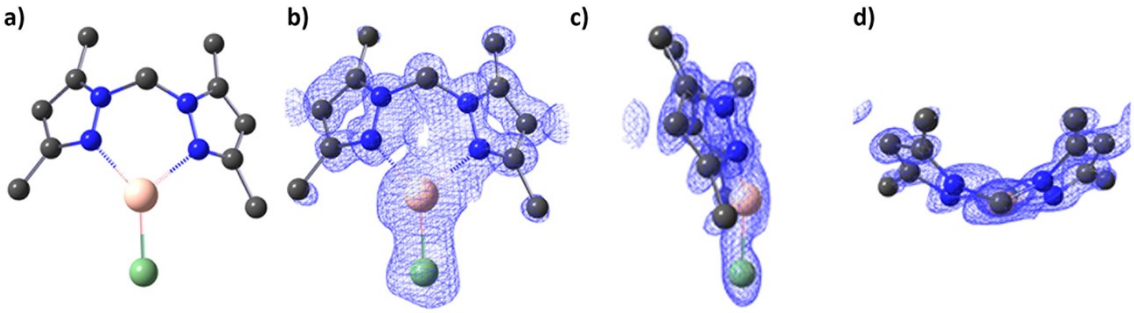

Figure S31. (a) Perspective view of the first chelated Cu(I) complex in **1**·[CuCl]-*locked*, and the overlaid electron density map as viewed from the (b) front, (c) side and (d) top of the complex.

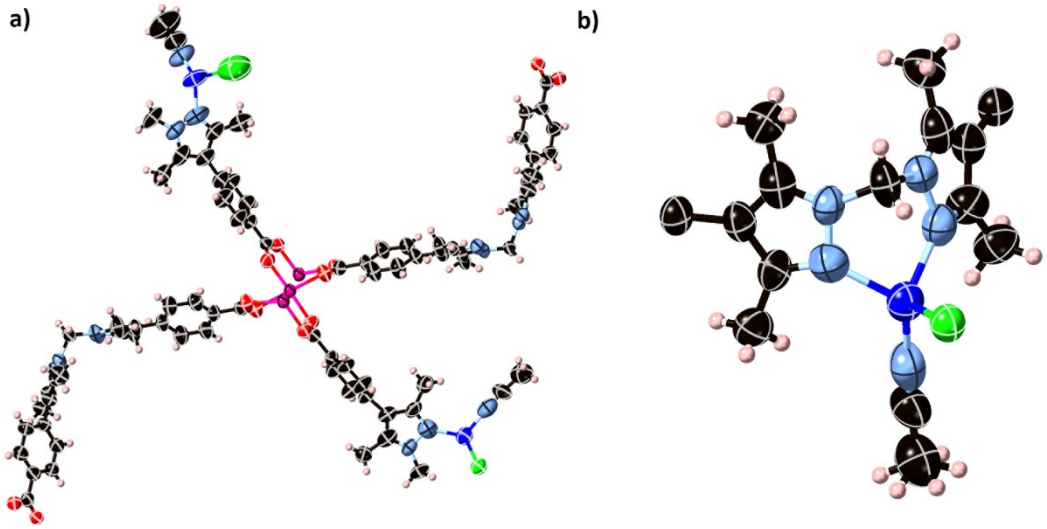

Figure S32. (a) The asymmetric unit of **1**·[CuCl]-*resolv* after first activating at 100 °C from *n*-pentane for 90 min (**1**·[CuCl]-*digonal*), and then resolvating in MeCN for 2 hours. All non-hydrogen atoms are represented by ellipsoids at the 50% probability level (C, black; H, white; N, light blue; O, red; Cu, dark blue; Mn, pink; Cl, green). Crystallographically resolved solvent molecules (MeCN) were removed for clarity. (b) Perspective view of the crystallographically distinct Cu(I) chelation sites with all non-hydrogen atoms represented by ellipsoids at the 50% probability level.

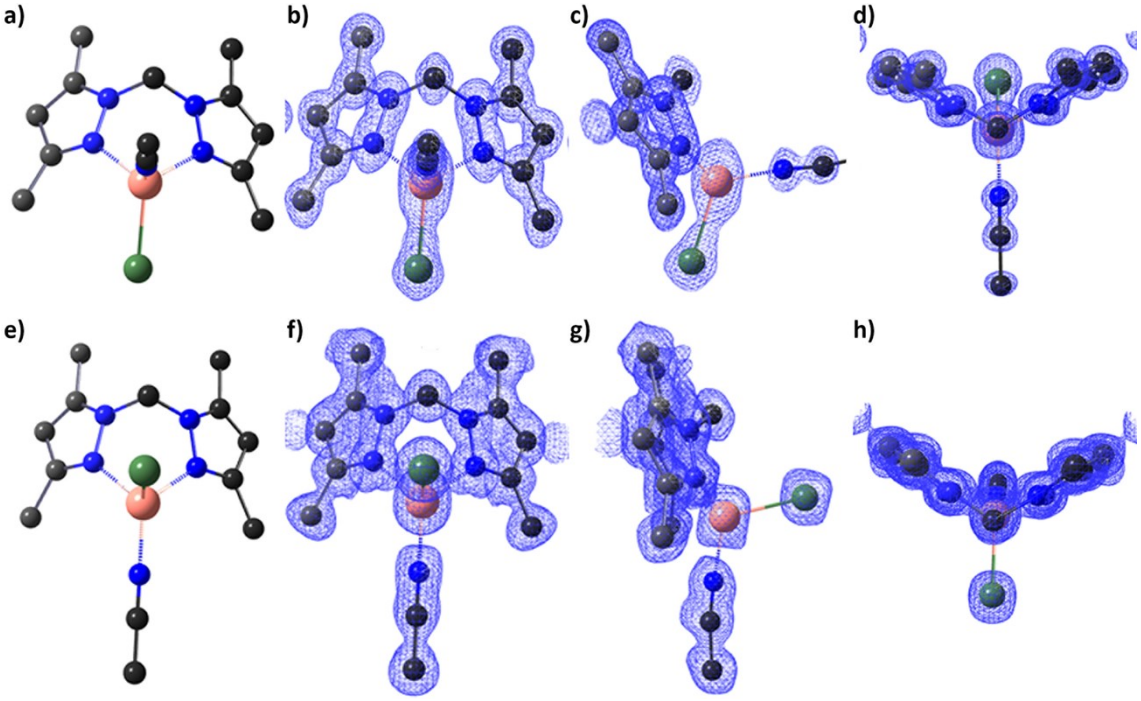

Figure S33. (a,e) Perspective view of the two crystallographically-defined chelated Cu(I) complex in **1**·[CuCl]-*resolv*, and the overlaid electron density map as viewed from the (b,f) front, (c,g) side and (d,h) top of the complexes.

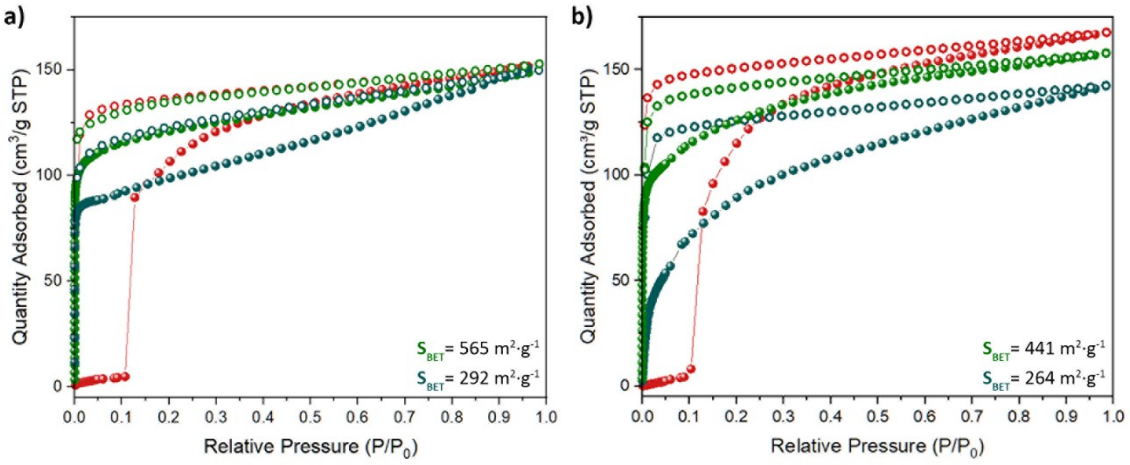

Figure S34. N_2 isotherm data cycle collected on the same batch of **1**·[CuCl] at 77 K from (a) dry diethyl ether, and (b) supercritical CO_2. Colour scheme: Initial isotherm of as-made material (green, **1**·[CuCl]-*locked*), heated at 100 °C for 90 minutes after the first isotherm (red, **1**·[CuCl]-*unlocked*), and third isotherm collected after resolvating for 2 hours in dry MeCN (**1**·[CuCl]-*resolv*) and washing with the corresponding solvent (dark green). Activation conditions: room temperature activation under vacuum, 90 min. Coloured circles represent adsorption, open circles represent desorption.

S2.0 Scanning Electron Microscopy (SEM) imaging

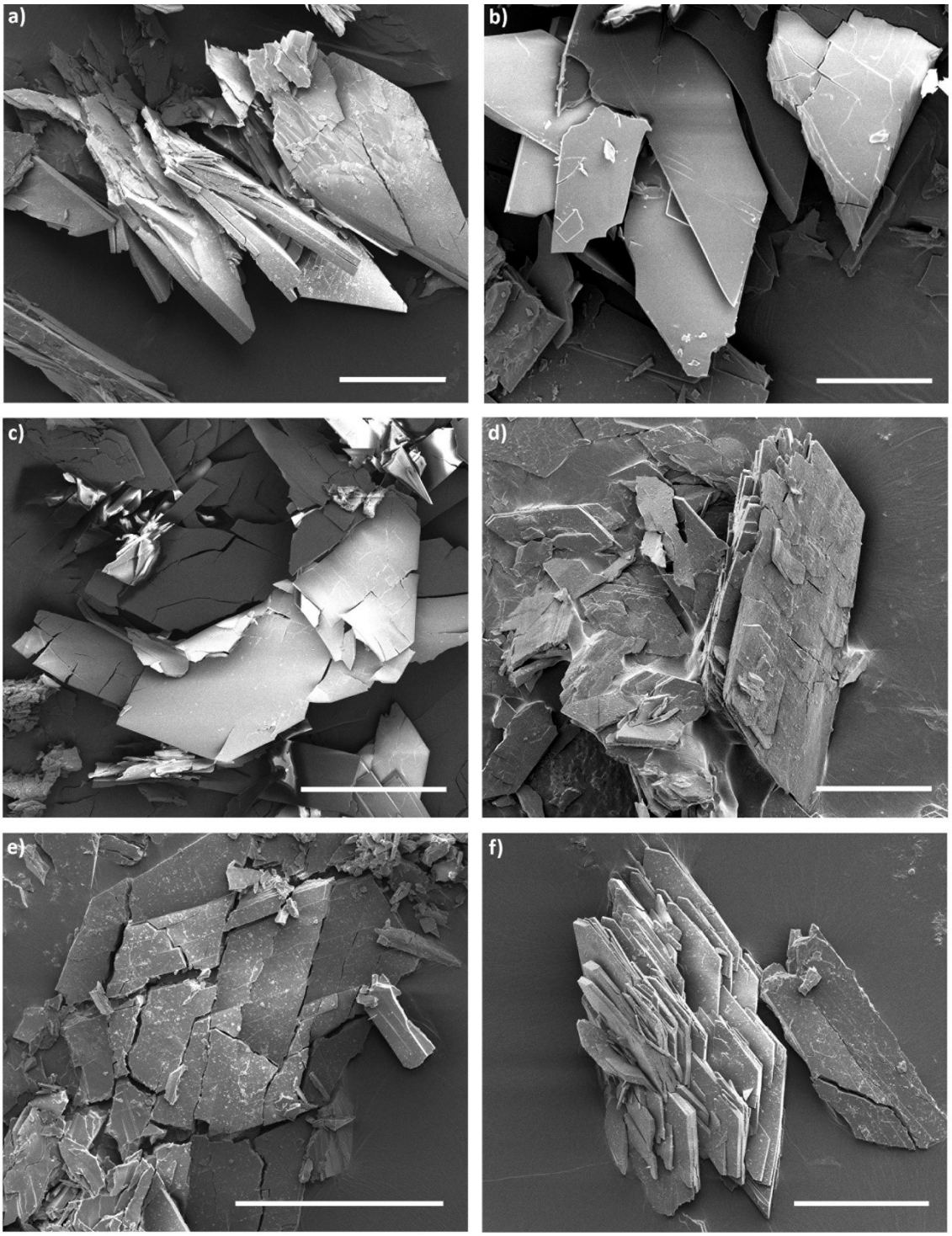

Figure S35. Representative HR-SEM images of (a) **1**·[CuCl], (b) **1**·[CuBr], (c) **1**·[CuI], (d) **1**·[CuCl]-*locked*, (e) **1**·[CuCl]-*unlocked*, and (f) **1**·[AuCl]. The samples were coated with a 3 nm Pt layer to reduce the visual aberrations caused by their poor electron conductivity. EDX quantification was performed to non-coated samples. Scale bars: 150 µm.

S3.0 Powder X-ray Diffraction (PXRD)

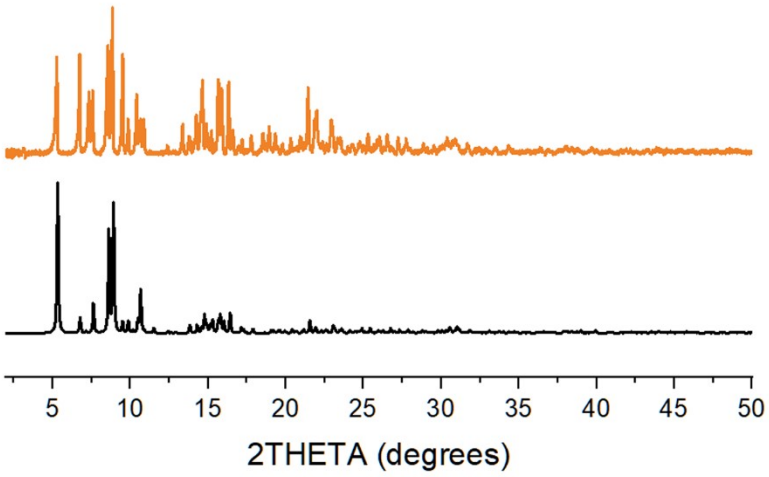

Figure S36. Experimental (top) versus simulated (100 K, bottom) PXRD plots for as-made **1**·[CuCl] (room temperature, trigonal planar). The flexibility of the framework causes slight shifts in the PXRD peak positions and intensity upon changes in solvation, activation, temperature, and potential oxidation during sample preparation (mortar grinding) for capillary PXRD.

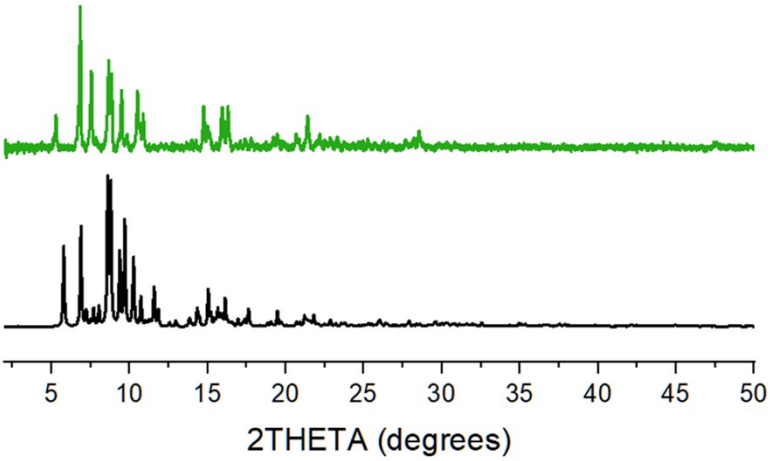

Figure S37. Experimental (top) versus simulated (100 K, bottom) PXRD plots for activated **1**·[CuCl]-*locked* (supercritical CO_2, trigonal planar). The flexibility of the framework causes slight shifts in the PXRD peak positions and intensity upon changes in solvation, activation, temperature, and potential oxidation during sample preparation (mortar grinding) for capillary PXRD.

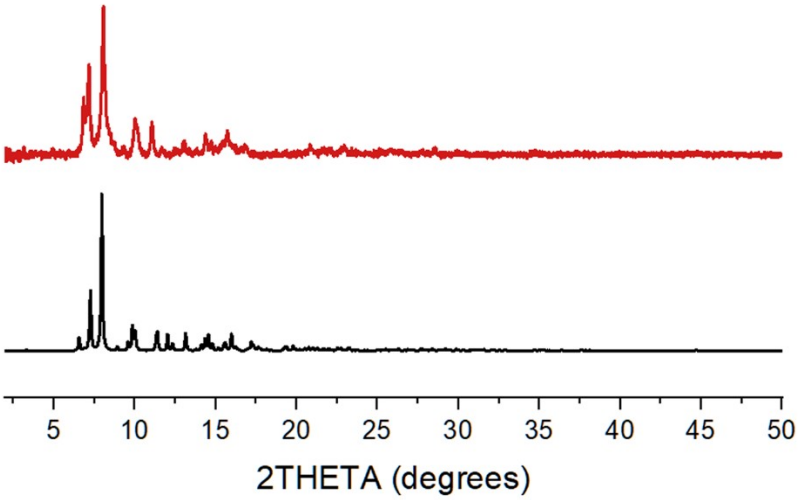

Figure S38. Experimental (top) versus simulated (100 K, bottom) PXRD plots for activated **1**·[CuCl]-un*locked* (100 °C from *n*-pentane, linear). The flexibility of the framework causes slight shifts in the PXRD peak positions and intensity upon changes in solvation, activation, temperature, and potential oxidation during sample preparation (mortar grinding) for capillary PXRD.

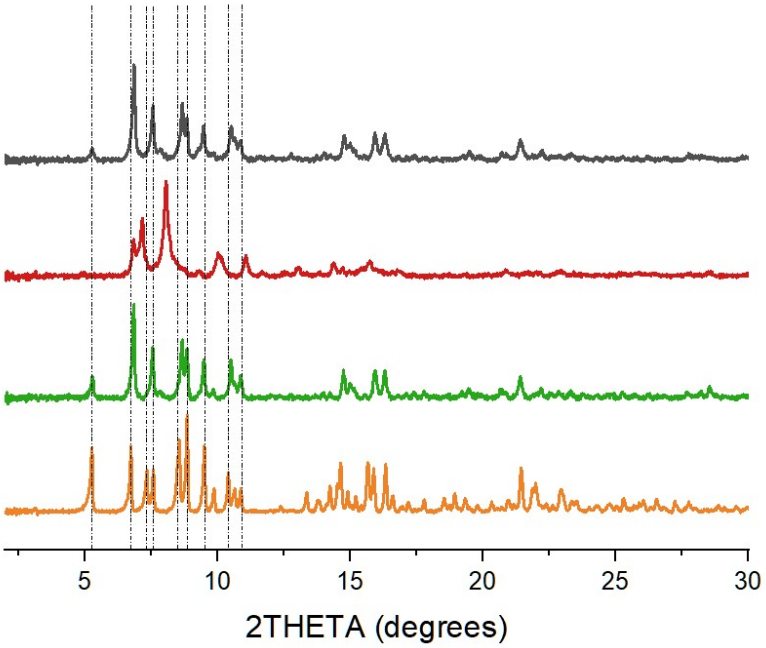

Figure S39. Low-angle experimental PXRD plots for as-made **1**·[CuCl] (orange), **1**·[CuCl]-*locked* (green), **1**·[CuCl]-*unlocked* (red), and **1**·[CuCl]-*resolv* (black). Dotted lines highlight the clear shifts in peak position upon phase transition from trigonal planar to linear, and the recovery of the initial structure upon resolvation. The flexibility of the framework causes slight shifts in the PXRD peak positions and intensity upon changes in solvation, activation, temperature, and potential oxidation during sample preparation for PXRD.

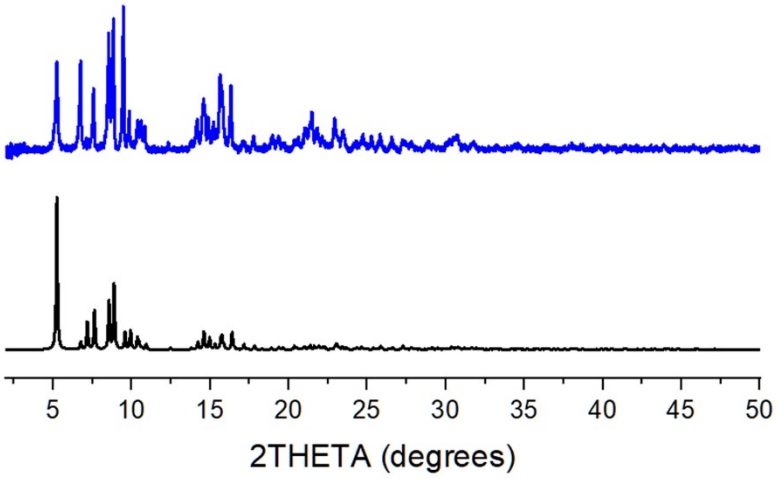

Figure S40. Experimental (top) versus simulated (100 K, bottom) PXRD plots for **1**·[CuBr]. The flexibility of the framework causes slight shifts in the PXRD peak positions and intensity upon changes in solvation, activation, temperature, and potential oxidation during sample preparation (mortar grinding) for capillary PXRD.

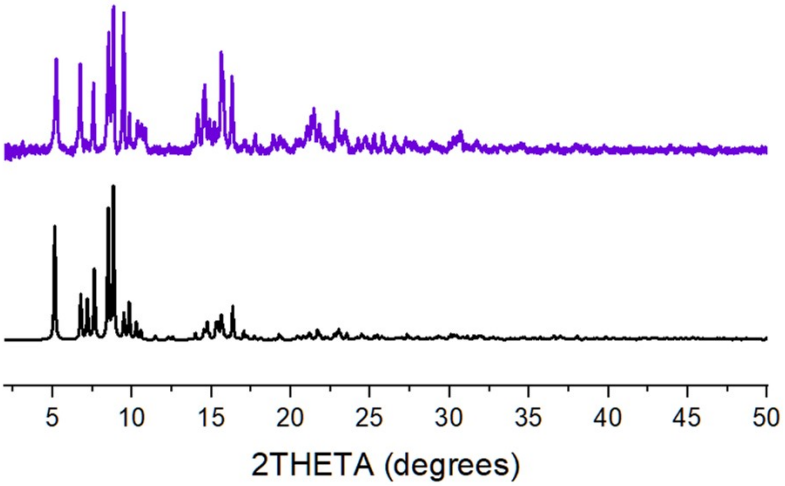

Figure S41. Experimental (top) versus simulated (100 K, bottom) PXRD plots for **1**·[CuI]. The flexibility of the framework causes slight shifts in the PXRD peak positions and intensity upon changes in solvation, activation, temperature, and potential oxidation during sample preparation (mortar grinding) for capillary PXRD.

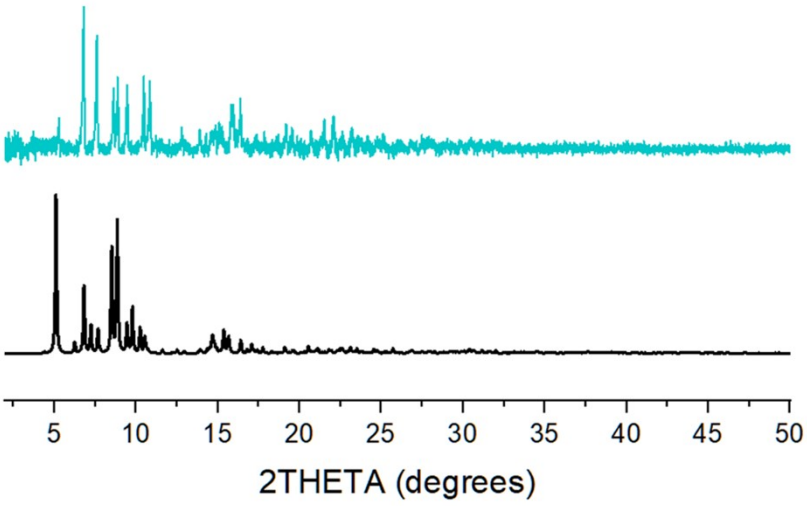

Figure S42. Experimental (top) versus simulated (100 K, bottom) PXRD plots for **1**·[AuCl]. The overall instability of the linear AuCl complex within the framework causes drastic shifts in the PXRD peak positions upon oxidation during sample preparation (mortar grinding) for capillary PXRD.

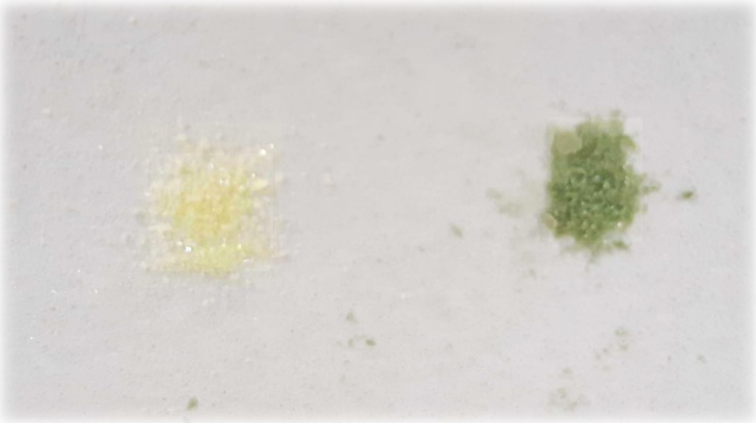

Figure S43. Photography of **1**·[CuCl] crystals before (yellow, left) and after (green, right) being exposed to air for 30 minutes. All the Cu(I) complexes embedded within the MOF are air sensitive, and thus all the PXRD measurements suffer from slight-to-moderate peak shifts attributed to the slow oxidation over time.

S4.0 Single crystal X-ray diffraction

S4.1 General Procedure

Single-crystals of **1** were mounted in Paratone-N oil on a MiTeGen micromount. SCXRD data was collected at 100 K on the MX1 or MX2 beamlines of the Australian Synchrotron using the Blue-ice software interface,[6] λ = 0.71073 Å. Absorption corrections were applied using multiscan methods using XDS,[7,8] the structures solved using SHELXS or SHELXT,[9,10] and refined by full-matrix least squares on F^2 by SHELXL,[11] interfaced through the program X-Seed or Olex2.[12,13] In general, all atoms were refined anisotropically and hydrogens atoms were included as invariants at geometrically estimated positions, unless specified otherwise in additional details in supporting information. Where noted, the data was treated with the SQUEEZE routine available in Platon[14] or using the solvent masking feature of Olex2. Figures were produced using the programs CrystalMaker and Diamond. X-ray experimental data is given in Table S4. CIF data have been deposited with the Cambridge Crystallographic Data Centre, CCDC reference numbers CCDC 2100590 - 2100596.

The structures reported in this manuscript are all metal-organic framework structures whose crystals:

- are prepared in multi-step crystal-to-crystal reaction sequences involving numerous solvent washing steps, chemical reactions, anion exchanges, or strong vacuum activation conditions;
- are weakly diffracting (all data collections reported were obtained at a synchrotron facility, including in some cases on an undulator based beamline, which provides additional flux);
- have a binding site that has the capacity to be disordered (and typically shows a small contribution of a disorder site in most of the reported structures); and,
- has significant diffuse scattering from solvent, anions, and other guests in the pore network.

These factors all create challenges for the structure determination and are shown by a handful of level A/B alerts registered by standard checking software. In addition, standard measures of refinement, such as R_1, wR_2 and GooF can be higher than typical crystals of close-packed inorganic structures, which can flag additional alerts. All A-level alerts are addressed in the cif files that are submitted and most level B-alerts relate to similar issues with the data collection, data quality or structural models and hence were not explicitly noted.

S4.2 Specific Refinement Details

1·[Cu(MeCN)(Cl)]. This structure has already been covered in one of our recent publications (CCDC file: 2071195).[15] Briefly, the coordination environment of the added [Cu(MeCN)(Cl)] moieties (two independent positions with different coordination environments) are significantly disordered. A series of SIMU, RIGU, and ISOR restraints were used to allow the refinement.

1·[CuCl]. There is some disorder of the metalation site in this material. This was modelled using SIMU and RIGU commands, and the methylene bridge of the ligand backbone modelled with a ISOR restraint. One toluene solvate molecule was located in the pores and was refined with the assistance of SIMU and RIGU commands. The solvent masking routine of Olex2 was used to account for electron density pertaining to two additional toluene molecules.

1·[CuCl]-*locked*. This is a sample that has been activated from diethyl ether and the crystal quality has been significantly impacted. The measures of data quality (intensity, R_{int}, completeness to standard theta limits) are impacted. There is some disorder of the metalation site in this material. This was modelled using SIMU and RIGU commands, and DFIX restraints on the pyrazole rings. The solvent masking routine of Olex2 was used to account for electron density pertaining to 3.75 diethyl ether molecules.

1·[CuCl]-*unlocked.* This is a sample that has been activated from pentane and the crystal quality has been severely impacted. The measures of data quality (intensity, R_{int}, completeness to standard theta limits) are impacted. There is some disorder of the metalation site in this material but more importantly the "anti" arrangement of the pyrazole donors mean the CuCl metal site is disordered over two main positions and cannot be located in the difference map (data collected on **1**·[CuCl]-*resolv*., below, supports this interpretation as the CuCl moiety is still present in the structure). This was modelled using SIMU and RIGU commands for all C, N and O atoms, and DFIX restraints on parts of several aromatic rings and ISOR restraints on the metal sites. The solvent masking routine of Olex2 was used to account for electron density pertaining to 2.5 pentane molecules and the CuCl moiety that cannot be located in the difference map.

1·[CuCl]-*resolv.* Resolvation of the crystals **1**·[CuCl]-*unlocked* with acetonitrile intriguingly significantly improves data quality and more importantly the ordering of the metalation site (this structure is more ordered than the starting material **1**·[Cu(MeCN)(Cl)]. A small number of DFIX and ISOR restraints were used for the chloride and acetonitrile ligands coordinated to the copper(I) metalation site.

1·[CuBr]. There is some disorder of the metalation site in this material. This was modelled using DFIX restraints for the methyl groups of the pyrazoles. One cyclohexane solvate molecule was located in the pores and was refined with the assistance of DFIX and ISOR commands. The solvent masking routine of Olex2 was used to account for electron density pertaining to one additional cyclohexane molecule. Crystal quality was affected by the post-synthetic anion exchange protocol meaning measures of data quality (intensity, R_{int}, completeness to standard theta limits) are severely impacted.

1·[CuI]. The weak diffraction, even from synchrotron radiation, made refinement difficult. SIMU and RIGU commands for all C, N and O atoms, ISOR and DFIX restraints were required to facilitate refinement of the structure. The solvent masking routine of Olex2 was applied as there is a significant void (658 $Å^3$) however the weak data meant that very limited electron density to be accounted for in the structure. Crystal quality was affected by the post-synthetic anion exchange protocol meaning measures of data quality (intensity, R_{int}, completeness to standard theta limits) are impacted.

1·[AuCl]. Extensive SIMU, RIGU and DFIX restraints were required to applied for the metalation site to facilitate refinement of the structure. The AuCl moiety appears to be disordered in the structure, but the supporting disorder of the metalation site (the ligand) could not be modelled. The solvent masking routine of Olex2 was used to account for electron density pertaining to 3.25 toluene solvate molecules.

S4.3 Crystallographic Tables

Table S4. Crystallographic data collection and refinement parameters for the metalated forms of MnMOF-1.

Sample	1·[CuCl]	1·[CuBr]	1·[CuI]	1·[CuCl]-*locked*
Formula	$C_{89}H_{82}N_{12}O_{12}Mn_3CuCl$	$C_{87}H_{90}BrCuMn_3N_{12}O_{12}$	$C_{75}H_{66}CuIMn_3N_{12}O_{12}$	$C_{75}H_{66}ClCuMn_3N_{12}O_{12}$
FW	1775.47	1803.97	1682.65	1591.20
T, K	150(2)	100(2)	150(2)	100(2)
Crystal System, Space Group	Monoclinic, $P2_1/m$	Monoclinic, $P2_1/m$	Monoclinic, $P2_1/m$	Triclinic, P-1
a, Å	12.3865(6)	12.335(3)	12.334(2)	12.308(3)
b, Å	33.158(2)	33.732(7)	34.440(8)	12.898(3)
c, Å	13.0706(6)	13.089(3)	13.084(2)	30.822(6)
α, °	90	90	90	94.70(3)
β, °	94.014(4)	93.23(3)	94.47(2)	95.44(3)
γ, °	90	90	90	92.66(3)
V, Å³	5355.1(5)	5437.5(19)	5541(2)	4847.3(17)
Z	2	2	2	2
ρ_{calc}, g/cm³	1.101	1.102	1.009	1.090
Absorption coefficient, mm^{-1}	0.621	0.953	0.848	0.679
F(000)	1834.0	1862.0	1706.0	1634.0
Crystal size, mm³	0.3 × 0.15 × 0.05	0.23 × 0.08 × 0.02	0.29 × 0.13 × 0.04	0.15 × 0.08 × 0.02
Wavelength	Mo Kα (λ = 0.71073)	Synchrotron (λ = 0.71073)	Mo Kα (λ = 0.71073)	Synchrotron (λ = 0.71073)
2Θ range for data collection, °	6.708 to 58.766	2.414 to 65.368	6.626 to 56.278	2.664 to 57.442
Index ranges	-16 ≤ h ≤ 16, -44 ≤ k ≤ 44, -17 ≤ l ≤ 17	-17 ≤ h ≤ 17, -45 ≤ k ≤ 45, -17 ≤ l ≤ 17	-16 ≤ h ≤ 16, -44 ≤ k ≤ 25, -12 ≤ l ≤ 16	-14 ≤ h ≤ 14, -16 ≤ k ≤ 16, -35 ≤ l ≤ 36
Reflections collected	63186	60121	19217	51592
Independent reflections	13398 [R_{int} = 0.1769, R_{sigma} = 0.2280]	13272 [R_{int} = 0.1533, R_{sigma} = 0.1440]	10966 [R_{int} = 0.3740, R_{sigma} = 0.9529]	17139 [Rint = 0.1554, Rsigma = 0.1757]
Data/restraints/parameters	13398/169/544	13272/43/562	10966/494/401	17139/254/951
GOF on F²	1.019	1.094	0.955	0.990
R_1, [I>=2σ (I)]	R_1 = 0.0999, wR_2 = 0.2585	R_1 = 0.1624, wR_2 = 0.4192	R_1 = 0.1917, wR_2 = 0.4391	R_1 = 0.1375, wR_2 = 0.3446
wR_2 [all data]	R_1 = 0.1897, wR_2 = 0.3044	R_1 = 0.2891, wR_2 = 0.4936	R_1 = 0.5056, wR_2 = 0.5919	R_1 = 0.2104, wR_2 = 0.4077
Largest diff. peak/hole, eÅ^{-3}	1.45/-1.60	1.08/-0.77	1.79/-0.67	0.93/-1.29
CCDC number	2100594	2100592	2100590	2100591

Table S4. Crystallographic data collection and refinement parameters for the metalated forms of MnMOF-1.

Sample	1·[CuCl]-*unlocked*	1·[CuCl]-*resolv*	1·[AuCl]
Formula	$C_{75}H_{66}Mn_3N_{12}O_{12}$	$C_{78}H_{70.5}ClCuMn_3N_{13.5}O_{12}$	$C_{75}H_{66}Au_{0.65}Cl_{0.65}Mn_3N_{12}O_{12}$
FW	1492.22	1652.78	1643.28
T, K	100(2)	100(2)	100(2)
Crystal System, Space Group	Triclinic, P-1	Monoclinic, $P2_1/m$	Monoclinic, $P2_1/c$
a, Å	12.341(3)	12.374(3)	13.026(3)
b, Å	12.924(3)	32.954(7)	34.629(7)
c, Å	27.121(5)	25.956(5)	24.547(5)
α, °	96.83(3)	90	90
β, °	91.48(3)	94.92(3)	95.71(3)
γ, °	90.60(3)	90	90
V, Å^3	4293.1(15)	10545(4)	11018(4)
Z	2	4	4
ρ_{calc}, g/cm^3	1.154	1.041	0.991
Absorption coefficient, mm^{-1}	0.493	0.626	1.262
F(000)	1542.0	3400.0	3334.0
Crystal size, mm^3	0.18 × 0.09 × 0.03	0.16 × 0.09 × 0.02	0.16 x 0.06 x 0.02
Wavelength	Synchrotron (λ = 0.71073)	Synchrotron (λ = 0.71073)	Synchrotron (λ = 0.71073)
2Θ range for data collection, °	3.174 to 58.712	1.574 to 57.286	2.04 to 64.212
Index ranges	-16 ≤ h ≤ 16, -17 ≤ k ≤ 17, -32 ≤ l ≤ 32	-16 ≤ h ≤ 16, -41 ≤ k ≤ 41, -34 ≤ l ≤ 34	-18 ≤ h ≤ 18, -46 ≤ k ≤ 46, -32 ≤ l ≤ 32
Reflections collected	51874	128693	190059
Independent reflections	15879 [R_{int} = 0.1806, R_{sigma} = 0.2144]	21566 [R_{int} = 0.0890, R_{sigma} = 0.0510]	28690 [R_{int} = 0.1383, R_{sigma} = 0.0911]
Data/restraints/parameters	15879/1478/870	21566/13/1022	28690/262/946
GOF on F^2	1.053	1.186	1.043
R_1, [I>=2σ (I)]	R_1 = 0.1789, wR_2 = 0.4393	R_1 = 0.1106, wR_2 = 0.3192	R1 = 0.1194, wR2 = 0.3392
wR_2 [all data]	R_1 = 0.2557, wR_2 = 0.5042	R_1 = 0.1478, wR_2 = 0.3501	R1 = 0.1584, wR2 = 0.3639
Largest diff. peak/hole, eÅ^{-3}	0.45/-0.70	1.50/-1.44	1.19/-1.30
CCDC number	2100593	2100595	2100596

S4.0 References

1. A. D. Becke, *Phys. Rev. A*, 1988, **38**, 3098.

2. J. P. Perdew, *Phys. Rev. B*, 1986, **33**, 8822.

3. F. Neese, F. Wennmohs, A. Hansen and U. Becker, *Chem. Phys.*, 2009, **356**, 98–109.

4. F. Weigend and R. Ahlrichs, *Phys. Chem. Chem. Phys.*, 2005, **7**, 3297–3305.

5. F. Weigend, Phys. *Chem. Chem. Phys*., 2006, **8**, 1057–1065.

6. T. McPhillips, S. McPhillips, H. Chiu, A. E. Cohen, A. M. Deacon, P. J. Ellis, E. Garman, A. Gonzalez, N. K. Sauter, R. P. Phizackerley, S. M. Soltis, P. Kuhn, *J. Synchrotron Radiat.*, 2002, **9**, 401-406.

7. N. P. Cowieson, D. Aragao, M. Clift, D. J. Ericsson, C. Gee, S. J. Harrop, N. Mudie, S. Panjikar, J. R. Price, A. Riboldi-Tunnicliffe, R. Williamson, T. Caradoc-Davies, *J. Synchrotron Radiat.*, 2015, **22**, 187-190.

8. D. Aragao, J. Aishima, H. Cherukuvada, R. Clarken, M. Clift, N. P. Cowieson, D. J. Ericsson, C. L. Gee, S. Macedo, N. Mudie, S. Panjikar, J. R. Price, A. Riboldi-Tunnicliffe, R. Rostan, R. Williamson, T. T. Caradoc-Davies, *J. Synchrotron Rad.*, 2018, **25**, 885-891.

9. G. Sheldrick, *Acta. Crystallogr. A*, 2008, **64**, 112-122.

10. G. Sheldrick, *Acta. Crystallogr. A*, 2015, **71**, 3-8.

11. G. Sheldrick, Acta. *Crystallogr. C*, 2015, **71**, 3-8.

12. L. J. Barbour, *J. Supramol. Chem.*, 2001, **1**, 189-191.

13. O. V. Dolomanov, L. J. Bourhis, R. J. Gildea, J. A. K. Howard, H. Puschmann, *J. Appl. Crystallogr.*, 2009, **42**, 339-341.

14. A. L. Spek, *Acta. Crystallogr. C*, 2015, **71**, 9-18.

15. R.A. Peralta, M.T. Huxley, J. Albalad, C.J. Sumby and C.J. Doonan, *Inorg. Chem.*, 2021, Accepted Manuscript (DOI: 10.1021/acs.inorgchem.1c00849)